

Article

# Direct Cryo Writing of Aerogels via 3D Printing of Aligned Cellulose Nanocrystals Inspired by the Plant Cell Wall

Doron Kam <sup>1,2</sup>, Michael Chasnitsky <sup>3</sup>, Chen Nowogrodski <sup>1</sup>, Ido Braslavsky <sup>3</sup>, Tiffany Abitbol <sup>4</sup>, Shlomo Magdassi <sup>2,\*</sup> and Oded Shoseyov <sup>1,\*</sup>

<sup>1</sup> Department of Plant Sciences and Genetics in Agriculture, Robert H. Smith Faculty of Agriculture, Food and Environment, The Hebrew University of Jerusalem, Rehovot 76100, Israel; doron.kam@mail.huji.ac.il (D.K.); chen.nowo@mail.huji.ac.il (C.N.)

<sup>2</sup> Casali Center of Applied Chemistry, Institute of Chemistry, The Hebrew University of Jerusalem, Jerusalem 91904, Israel

<sup>3</sup> Institute of Biochemistry, Food Science and Nutrition, Robert H. Smith Faculty of Agriculture, Food and Environment, The Hebrew University of Jerusalem, Rehovot 76100, Israel; mishaches@gmail.com (M.C.); ido.braslavsky@mail.huji.ac.il (I.B.)

<sup>4</sup> RISE, Stockholm 114 28, Sweden; tiffany.abitbol@ri.se

\* Correspondence: magdassi@mail.huji.ac.il (S.M.); shoseyov@agri.huji.ac.il (O.S.)

Received: 20 February 2019; Accepted: 17 April 2019; Published: 19 April 2019



**Abstract:** Aerogel objects inspired by plant cell wall components and structures were fabricated using extrusion-based 3D printing at cryogenic temperatures. The printing process combines 3D printing with the alignment of rod-shaped nanoparticles through the freeze-casting of aqueous inks. We have named this method direct cryo writing (DCW) as it encompasses in a single processing step traditional directional freeze casting and the spatial fidelity of 3D printing. DCW is demonstrated with inks that are composed of an aqueous mixture of cellulose nanocrystals (CNCs) and xyloglucan (XG), which are the major building blocks of plant cell walls. Rapid fixation of the inks is achieved through tailored rheological properties and controlled directional freezing. Morphological evaluation revealed the role of ice crystal growth in the alignment of CNCs and XG. The structure of the aerogels changed from organized and tubular to disordered and flakey pores with an increase in XG content. The internal structure of the printed objects mimics the structure of various wood species and can therefore be used to create wood-like structures via additive manufacturing technologies using only renewable wood-based materials.

**Keywords:** nanocellulose; 3D printing; aerogels; ice templating; biomimetics

## 1. Introduction

Plants are fascinating engineering materials as they consist of multi-cellular architectures evolved by nature to serve a specific function [1]. The three main constituents of the plant cell wall are cellulose, hemicellulose, and lignin, each with its specific role. Cellulose is the most abundant polysaccharide in nature and is the main load-bearing element in plants, where cellulose polymer chains bundle together into microfibrils, consisting of highly crystalline and less crystalline regions, which then group together into fibers [2]. Hemicellulose is the second-most abundant polysaccharide in nature [3] and acts as the “glue” that binds cellulose microfibrils, while lignin interlaces with the cellulose–hemicellulose composite, forming a protective barrier against enzymes and microbes [4].

Freeze casting, also known as ice templating, enables the alignment of particles through directional freezing followed by sublimation, which results in cellular objects [5,6]. Various applications of

freeze-cast objects can be found in fields where an anisotropic geometry with complex and functional hierarchy is needed [7]. Among them are thermal insulators [8], high performance batteries [9], tough and highly compressible materials [10,11], and bone substitutes [12]. Wood, similar to other natural materials, has a sophisticated structure with different levels of hierarchical organization and properties that surpass typical manmade materials [13]. Therefore, mimicking nature is more than mixing and matching the right building blocks, but also using new technologies to put these elements together in a way that achieves architectures similar to the natural material.

The 3D printing of cellulose-based materials in the context of “hydrogel to aerogel” has emerged in the past few years, including in wound healing applications [14,15], scaffolds [16–18], lightweight foams [19], and aerogel substrates for supercapacitors [20]. Nanocellulose-containing hydrogels and aerogels, as well the different approaches used to prepare these materials and their applications, have been recently reviewed by De France et al. [21]. Different from previous approaches, this study presents the 3D printing of cell-wall building blocks to create bioinspired structures via direct cryo writing (DCW). The building blocks are rod-shaped cellulose nanocrystals (CNCs), extracted from plant fibers via hydrolysis [22], and a binder, xyloglucan (XG), the most abundant hemicellulose present in the cell walls of dicotyledonous plants [23].

CNCs are the crystalline elements extracted from the cellulose microfibrils in plant fibers. They possess many of the properties of native crystalline cellulose including high strength and insolubility in most solvents. However, CNCs extracted by sulfuric acid have anionic sulfate-half ester groups grafted onto their surfaces, a functionality that is non-native to natural cellulose but that imparts colloidal stability to aqueous CNC suspensions through electrostatic repulsive interactions that are key to the processing of CNCs into uniform materials. CNC size, surface charge type and magnitude, and crystallinity are governed by the source material and preparation conditions [24–26].

In the plant cell wall, the combination of cellulose and XG leads to physical entanglements that result in an extensible structure [27], where hydrogen bonding and van der Waals forces drive the binding of XG to cellulose surfaces and their crosslinking [28,29]. Recent studies of the adsorption of XG extracted from tamarind onto CNC surfaces have demonstrated that the adsorption is kinetically driven, concentration dependent, and is accompanied by the release of bound water [30,31]. CNCs and XG have the potential to yield composites that biomimic the plant cell wall, as has been previously investigated in layer by layer (LbL) films [32,33].

Other researchers have used freeze casting to create porous materials from plant components; for example, aerogels were made from CNCs [34], nanofibrillated cellulose (NFC) [35], and microfibrillated cellulose (MFC) [36], and hydrogels from xylan [37]. The addition of XG to MFC was found to yield aerogels with ultra-high porosity and better mechanical properties compared with pure MFC aerogels [38]. Moreover, CNCs have been aligned by directional freezing to produce aligned foams [34], which are of interest due to the renewable and biocompatible nature of CNCs and the possibility to control long-range order in the final materials through processing [39]. The novelty of the current report is the use of a blend of CNC and XG to mimic the chemical composition of wood and the use of cryo-3D printing as an approach to capture the internal architecture of wood.

In the direct ink writing (DIW) printing process used in this study, a fluid is extruded through a nozzle to form a 2D pattern, a process that is then repeated to build-up 3D structures [40,41]. This process is extensively used in the field of bioprinting, which is an emerging field of research [42–44]. A major challenge inherent to this technology is the requirement of rapid fixation of the ink as soon as it is deposited onto the build platform in order to successfully attain the pre-designed shape. Rapid fixation can be accomplished by photopolymerization [45], thermal crosslinking [46], or tuning of the rheological properties of the ink [47]. A further challenge is the collapse of printed structures due to gravity, which is particularly relevant for angular geometries. This last limitation can be overcome by first printing a support material, but this approach is accompanied by additional challenges, such as the need for complicated multi-nozzle printers and post-processing to remove the support material. Rapid fixation can also be achieved via low-temperature deposition manufacturing (LDM) processes.

LDM for DIW can be categorized according to three main approaches: (1) printing in a cooled chamber, (2) printing onto a cooled stage, and (3) printing into a cooled liquid. Xiong et al. were first to report 3D printing with a polymer solution in a refrigerator for tissue engineering applications [48]. Kim et al. were first to use a cooled stage to cryogenically 3D print collagen scaffolds [49], Liao et al. developed a 3D printing system for tissue engineering applications using a temperature-controlled cold stage [50] and Adamkiewicz et al. 3D printed hydrogels into liquid nitrogen, also for tissue engineering [51]. Finally, drop on demand printing, another LDM process, was used by Zhang et al. to achieve graphene aerogels [52].

In this study, inspired by the plant cell wall structure, aerogels were prepared from aqueous mixtures of relatively low concentrations of CNCs (4 wt%) and XG using 3D printing via DCW to align the CNCs at cryogenic temperatures. Song et al. recently published the DCW of hydroxyapatite aqueous mixtures (above 60 wt%) for a bone cell culture by printing on a cold stage whose temperature was continually lowered throughout the process [53]. Here, we explore the combination of freeze casting and 3D printing for systems containing a relatively low concentration of cellulose nanocrystals while the freezing process is conducted with a feedback-based temperature control. Directly printing onto a temperature-controlled cold platform enables complex structures with tilted facets, without requiring any support material via proper coordination between the printing flowrate and the freezing rate. With the increase in height of the printed object, the platform temperature and the printing speed can be decreased, enabling the fabrication of a large overhang. The thermal gradients obtained by directional freezing enable the slow and directional growth of ice crystals within the structure, which drive the alignment of the CNCs. DCW allows simultaneous printing and freezing, effectively shortening the freezing process. The frozen objects are directly post-processed via lyophilization, resulting in 3D printed aerogels with aligned structures. These objects are proposed as superior thermal insulators for complex structures due to the 3D design freedom and the anisotropic aerogel structure. Moreover, the low solid content coupled together with porosity control and tunable architecture makes these objects interesting as custom designed biological scaffolds.

## 2. Materials and Methods

### 2.1. Materials

A cellulose nanocrystal (CNC) dispersion was prepared via sulfuric acid hydrolysis. Bleached, softwood kraft pulp (TEMBEC) was dried in a 60 °C oven for 48 h. Next, 40 g of the dried pulp was vigorously mixed with 700 mL of sulfuric acid (61 wt%) using mechanical stirring for 2.5 h in a water bath set to 50 °C. The reaction was then quenched via 10-fold dilution in chilled deionized water, followed by three washes via centrifugation (20 °C, 6000 rpm, Sorvall RC5C Plus, Kendro, Newtown, CT, USA) to remove excess acid. The CNCs were then dialyzed against distilled water (12–14 kDa, Medicell Membranes LTD, London, England) for at least two weeks with daily water changes, followed by sonication, filtration (Whatman 41 filter paper), and another round of centrifugation (5000 rpm, 10 min) to remove particulates introduced by the sonication probe. XG from tamarind seed was supplied by Megazyme (Bray, Ireland). XG solutions (2 and 4 wt%) were prepared via mixing XG in water for 2 h at 80 °C until dissolution was achieved. Different ratios of XG to CNCs were mixed using magnetic stirring for at least 1 h with the overall solid content maintained at 4 wt%.

### 2.2. Rheology

Rheology measurements were performed at room temperature (25 °C) using a Haake Rheostress 6000 Rheometer (Thermo Fisher Scientific, Waltham, MA, USA) coupled with a RS6000 temperature controller. The rheometer was operated in controlled rate (CR) mode, where the shear rate was fixed, while the shear viscosity was measured (lower plate—TMP 60, upper plate—P60 TiL; cone—plate geometry).

### 2.3. DCW 3D Printing of Aerogels

XG:CNC dispersions were 3D printed using a Hyrel3D 30M printer (Hyrel International, Inc., Norcross, GA, USA) equipped with an EMO-25 extruder (cold flow) mounted with an 18-gauge stainless steel tip. The HYREL3D 30M printer has a  $5 \times 5 \times 1 \mu\text{m}$  positional resolution, a  $50 \times 50 \times 10 \mu\text{m}$  positional accuracy, and a  $25 \times 25 \times 5 \mu\text{m}$  positional repeatability. It can be mounted with any needle, but the needle diameter becomes the upper bound for the layer height. A custom made cold platform was assembled from a copper plate attached with conductive grease to a standard thermoelectric cooler (TEC) mounted onto a water block heat exchanger ([customthermoelectric.com](http://customthermoelectric.com)) and controlled by a power supply (EA-PS 2042-20B, Elektro-Automatik). In addition, a FLIR E4 infrared camera (FLIR systems, Wilsonville, OR, USA) with a ZnSe lens (1" focal length) was used to acquire thermal images and temperatures along the printed object during the 3D printing. We monitored the advance of the ice front in the 3D printed object during printing, and based on that, we controlled the cooling of the stage by manually adjusting the current to the TEC, keeping the two top layers unfrozen.

G-code files were prepared via 3D Slic3r software (Ver. 1.2.9, [slic3r.org](http://slic3r.org)). The printing rate was set to 3 mm/s and the layer height was set to 0.8 mm to print cylindrical hydrogel specimens with a diameter of 10 mm and height of 5 mm. The frozen objects were lyophilized (Labconco Freezone 2.5, Kansas city, MO, USA) and stored in sealed vials until further testing.

### 2.4. Mechanical Properties

The mechanical properties of the 3D printed cylindrical aerogels (with an average height of 5 mm and a diameter of 10 mm) were evaluated in compression-mode using an Instron universal testing machine (Model 3345, Instron Corp., Norwood, MA, USA) equipped with a 100 N load cell and operated at 2 mm/min. Five replicate specimens were tested at ambient laboratory conditions.

### 2.5. Scanning Electron Microscopy (SEM)

The structures and morphologies of the 3D printed aerogels were imaged using a JEOL scanning electron microscope (model JSM-IT-100, Tokyo, Japan). Samples were placed onto carbon tape and mounted into a holder such that the cross sections were exposed to the beam. Prior to imaging, the samples were coated using a Quorum Q150T Iridium sputter (Quorum Technologies Ltd, Laughton, UK) coater to give a 2 nm layer and ensure sample conductivity. The images were captured at an accelerating voltage of 3 kV at a working distance of 11 mm.

### 2.6. Translational Cryostage

To observe the formation of ice crystals within the dispersions, samples were mounted into a custom-built translational cryostage, which has been described elsewhere [54]. Briefly, samples were placed between two glass slides on a copper plate and observed through a slit under an inverted microscope (IX51, Olympus, Tokyo, Japan). Two Peltier thermoelectric coolers (TEC) were maintained with a  $\Delta T$  of 4 °C ( $T_{\text{hot}} = 1 \text{ }^\circ\text{C}$ ,  $T_{\text{cold}} = -3 \text{ }^\circ\text{C}$ ) by a high precision proportional integral derivative (PID) temperature controller (PRO800 system with two TED8020 modules, ThorLabs, Newton, NJ, UDS).

### 2.7. Statistical Analyses

Three independent 1 mL measurements were obtained for the rheology measurements, but only one representative curve is presented in the results. Results are displayed on a log–log scale. As for the DCW printed from aerogels, ten replicates were printed from the five different ratios of XG to CNCs inks, out of which five were randomly selected for mechanical properties and imaging.

Young's modulus values were calculated from the stress–strain curves between 0–0.2 strain using MATLAB 2015a (MathWorks, Natick, MA, USA). An average plot of the five measurements with the associated standard error of the mean is presented.

### 3. Results and Discussion

DCW printing experiments were conducted via the extrusion of water-based XG:CNC compositions onto a temperature-controlled cold plate, allowing directional freezing from the plate upward into the sample, as is shown schematically in Figure 1a. The resultant frozen 3D hydrogel objects (Figure 1b) were post-processed using lyophilization, yielding 3D aerogels, as shown in a typical example (Figure 1c). Successful 3D printing of objects using an extrusion-based process can be achieved using ink compositions that have shear-thinning rheological properties. The shear thinning behavior of fluids describes how materials effectively become less viscous with applied stress, often reverting back toward their initial viscosity once the stress is removed [55]. This feature is critical to many applications, such as paints and coatings, and especially for extrusion-based 3D printing, where the material is required to flow easily as it is extruded but to remain in place once it has been deposited onto the build platform, thus fixing the material in its pre-designed shape. CNCs exhibit shear thinning behavior as well as relatively high viscosities at low shear and at relatively low concentrations [56,57], making this material a good candidate for water-based 3D printable inks [58]. In this study, we extracted CNCs using 61 wt% sulfuric acid, which is lower than typically used, resulting in low–moderate surface charge values ( $\approx 0.2$ – $0.5\%$  S, expressed as a sulfur content as charge groups are sulfate-half esters) as compared to commercial CNCs (0.66 to 1.1% S) [59]. Dispersions of lower surface charge CNCs in pure water are more viscous compared to dispersions of higher charged CNCs, and have viscosities that are sufficiently high for the successful 3D printing of CNC dispersions (even at relatively low solid concentrations) [60]. Recently, a CNC hydrogel (20 wt%) was used to fabricate aerogels via DIW, with a main focus of the work on the optimization of ink printability rather than on the micro-features of the freeze-dried material [61]. In the present report, we were able to print low concentration CNC hydrogels ( $<4$  wt%), which allowed for tuning of the porosity and internal alignment within the object. We expect that the high porosity may facilitate biocompatibility and accelerate biodegradation. Moreover, we expect that the aligned structures achieved due to the combination of XG with CNC may enable cell orientation templating, an important requirement for future printed implants.

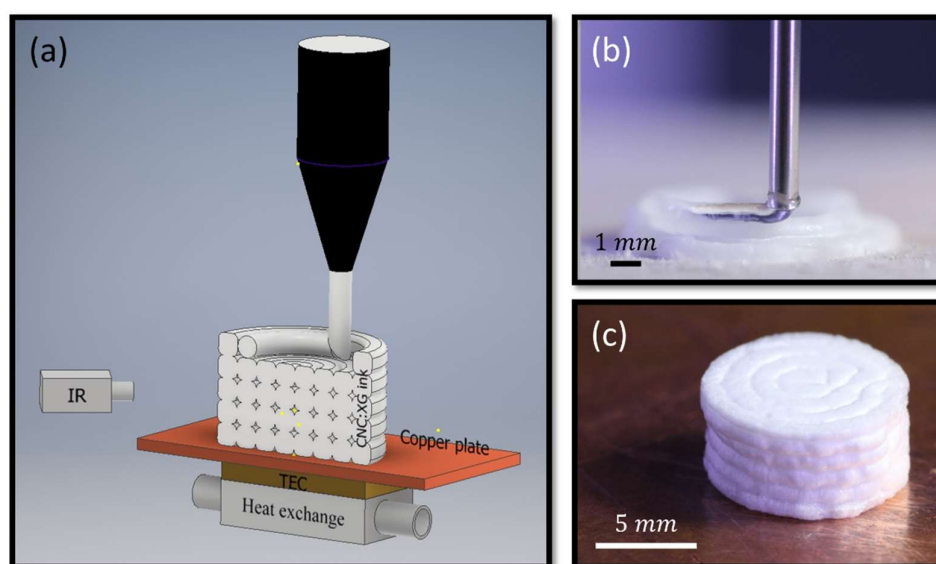


**Figure 1.** (a) Schematic illustration of the DCW setup, (b) photograph of the DCW printing process, and (c) of final aerogel.

#### 3.1. Rheology

The ink is composed of CNCs, cell-wall building blocks, which are combined with another cell-wall building block, xyloglucan (XG), which acts as a binder. Since this binder can also affect the rheology of the resulting ink, we evaluated the viscosity profiles of the inks composed at different mass

ratios of XG to CNC (4 wt% overall solids for all compositions). As shown in Figure 2, shear-thinning behavior was observed for all samples that contain CNCs, while the viscosity at any given shear rate was higher for higher XG concentrations. For instance, the viscosity of the pure CNC dispersion at 4 wt% (0:1 XG:CNC ratio) and at  $0.1 \text{ s}^{-1}$  was an order of magnitude lower compared to the 1:4 XG:CNC dispersion (i.e., 30 Pa·s versus 300 Pa·s). However, at high XG concentrations (1:4 and 1:10 XG:CNC), the gel structure collapsed as indicated by the curves at high shear rates. We note that although XG is a soluble polymer, pure solutions of XG at 4 wt% (the highest concentration tested and used in this work) exhibited Newtonian behavior, where viscosity is unaffected by shear.

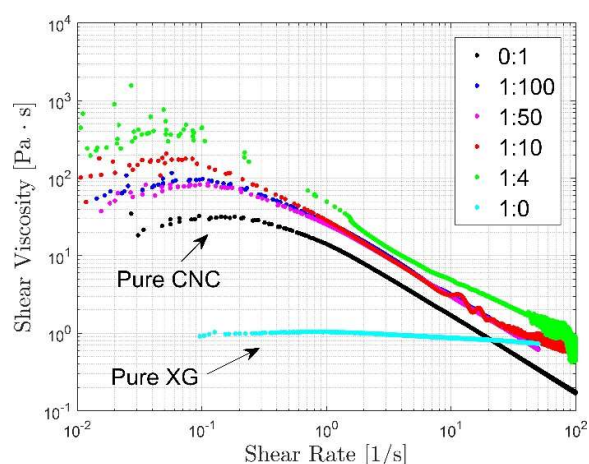


**Figure 2.** Viscosity measurements of mixtures of XG and CNCs at different ratios showing the influence of XG content on the overall viscosity and the shear thinning behavior of CNCs. Legend indicates the ratio of XG:CNC.

The increase in CNC viscosity due to the addition of XG is most likely related to the binding XG to the CNCs [62,63]. Eronen et al. studied the adsorption of XG and other hemicelluloses onto nanofibrillar cellulose and found that XG adsorption occurred to a greater extent compared with other hemicelluloses [64]. Moreover, a strong association between XG and CNCs has been demonstrated in LbL studies, where film thickness attained a constant value at high XG concentrations, whereas an unlimited linear build-up of bilayers was observed for dilute XG [65]. This observation suggests that at low concentrations XG acts as a crosslinking agent, whereas at high concentrations, XG exerts a slippery effect. The interactions between CNCs and XG resulted in surface coverage of CNCs by XG and bridging between CNCs, phenomena that potentially explain the increase in viscosity observed when XG was added to a CNC dispersion. Thus, the XG in our system mimicked its role in the plant cell wall by “gluing” together cellulosic building blocks into 3D objects and also acted as a rheological modifier. The following printing experiments were conducted with samples comprised of both CNCs and XG (pure XG was excluded due to its Newtonian behavior).

### 3.2. DCW 3D Printing of Aerogels

We first printed a pure CNC dispersion (0:1 XG:CNC, 4 wt%) via DIW without freezing to demonstrate that this extrusion-based technique can be used for printing relatively low concentrations of CNCs (Figure S1). However, as is seen in Figure S1, the resultant object (cylinder height and diameter = 5 mm) was slightly distorted, demonstrating the need for rapid fixation as was discussed previously. Therefore, in subsequent experiments, the challenge of fixation was tackled through a combination of the shear-thinning rheology of CNCs coupled with immediate directional freezing. We emphasize that in the absence of freezing, objects printed and dried under ambient conditions from CNC dispersions simply collapse into films.

The ink compositions containing both CNCs and XG were 3D printed using DCW (4 wt% overall solids) and the resultant printed objects were lyophilized to obtain 3D printed aerogels (discussed

below in more detail). As indicated above, DCW subjects the deposited samples to a temperature gradient, where temperatures gradually increase further into the printed object, away from the temperature-controlled cooling plate, resulting in directional ice crystal growth in the vertical direction. We note that a cooling platform kept at a constant temperature is expected to result in uneven ice crystal growth throughout the printing process due to the increasing distance between the cold surface and the printed layers. To preserve the ice growth rate as the 3D structure evolves, the temperature of the platform is lowered throughout the printing process and the freezing rate is tuned to avoid either fast or slow ice growth. Rapid ice growth results in the deposition of liquid ink on top of an already completely frozen layer, causing poor adhesion between discrete 2D layers. Conversely, slow ice growth leads to longer printing times and distortion of the shape of the printed structure.

A balance between the two mechanisms of fixation is therefore required. Appropriate rheological properties of the ink as well as maintaining control of the ice growth rate within the sample throughout printing by rapid adjustment of the temperature of the platform are essential.

To maintain continuous ice growth throughout the printed layers, the inks were extruded onto a Peltier plate, whose temperature could be rapidly and efficiently controlled. A thermal camera was used for feedback to control the temperature by monitoring the height of the 0 °C plane, which corresponds to the plane of the ice growth front, such that a continuous thin liquid layer was maintained on top of the frozen sample throughout the entire printing process. This liquid phase was approximately one printed layer thick, quantified via thermal imaging (Figure 3). Practically, the rate of ice growth was monitored and the temperature of the platform was adjusted as the sample was printed. This setup enabled the cryo-3D printing of CNC-based inks by depositing a liquid sample directly onto the cold stage in the first layer, followed by printing onto the unfrozen top layer in subsequent layers without disruption to the underlying ice crystal growth, which is key to CNC alignment within the structure [34,66].

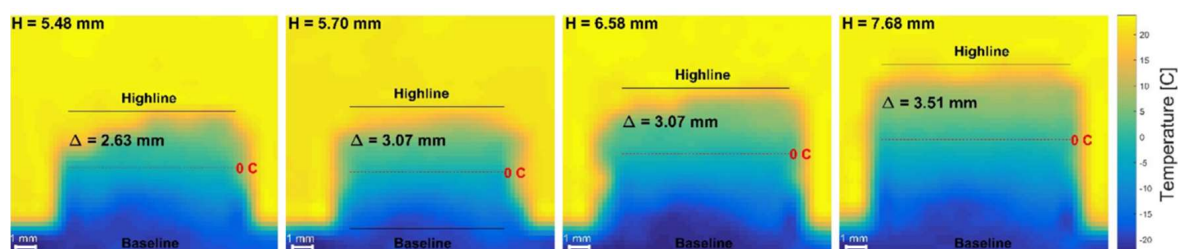


**Figure 3.** An example of the thermal imaging obtained while 3D printing layers of an XG:CNC (1:100) ink. The height (H) of the sample and the thickness of the top layer of liquid that had not yet been frozen ( $\Delta$ ) are indicated.

### 3.3. Scanning Electron Microscopy (SEM)

SEM of sample cross-sections was used to image the morphologies of the 3D DCW printed aerogels at right-angle (tangential) and parallel (longitudinal) positions to the cold stage. Figure 4 presents tangential cross-sectional SEM images of the 3D printed aerogels at five XG:CNC ratios. Neither voids nor cylindrical filament shapes were present between layers, indicating that continuous ice crystal growth and homogenous freezing was indeed achieved within these printed objects. Moreover, the pure CNC sample exhibited a lamellar morphology (Figure 4b) that evolved into a tubular structure as more XG was included in the ink (Figure 4c,d), until eventually the structure of the aerogel became disordered (Figure 4e,f). Longitudinal cross-sectional SEM images showed that the pure CNC sample had an organized lamellar structure (Figure 5b), the 1:100 XG:CNC sample had an open-cell foam structure (Figure 5c), and the 1:50 XG:CNC sample (Figure 5d) had an ordered tubular structure that eventually degraded to a flakey structure with further increases in XG content (Figure 5e,f).

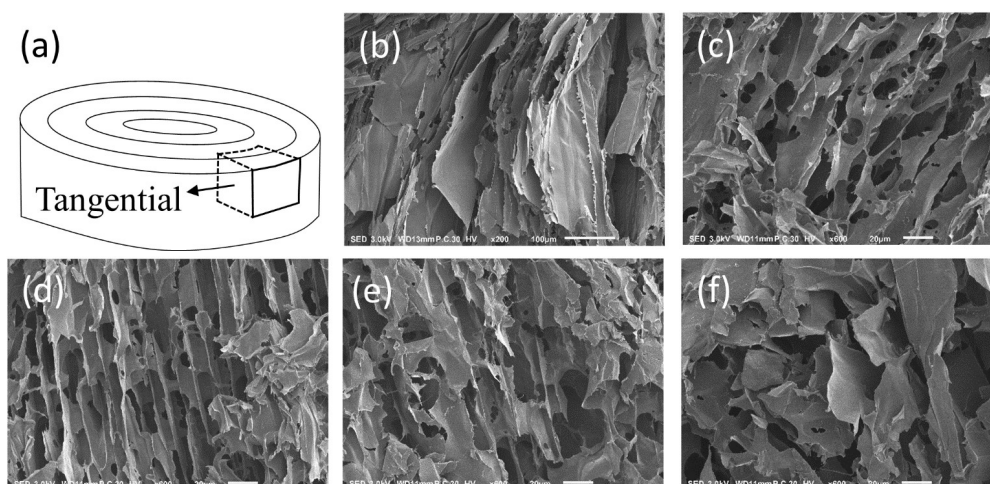


**Figure 4.** Cross-sectional SEM images of 3D printed aerogels in the tangential direction, vertical to the cold stage: (a) schematic of the direction of the observation and (b–f) SEM images of aerogels prepared from different XG:CNC ratios 0:1, 1:100, 1:50, 1:10, and 1:4, respectively.

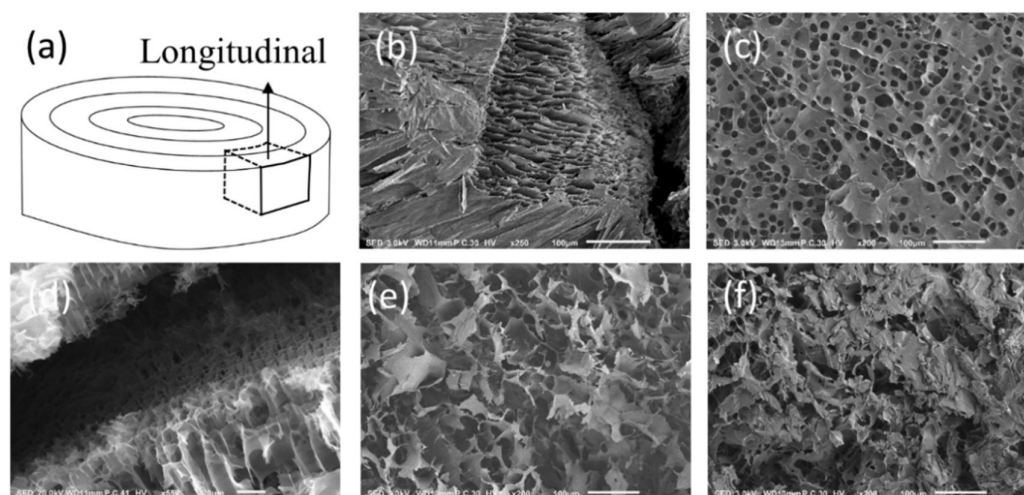


**Figure 5.** Cross-sectional SEM images in the longitudinal direction parallel to the cold stage: (a) schematic of the direction of the observation and (b–f) SEM images of aerogels prepared from different XG:CNC ratios of 0:1, 1:100, 1:50, 1:10, and 1:4, respectively.

To assess the quality of the 3D printed samples, we printed a sample using suboptimal settings; a 0.1 mm line space gap was introduced between each printing path and printing was performed at a constant platform temperature of  $-20\text{ }^{\circ}\text{C}$  (Figure S2). Poor adhesion can be seen between layers, as well as a printed filament with a circular cross-section, which is indicative of an inappropriately large spacing between lines. Overall, the cross-sectional SEM images (Figures 4 and 5) indicate that the inks were continuously printed to give bulk and homogeneous 3D structures, which had no discernible layers. Additionally, these images show that the internal structure of the resultant aerogels could be tuned by controlling the ratio of XG to CNC, from lamellae to tubes to disordered flakes, with increasing XG concentration.

Interestingly, cross-sectional images of wood structures show a similar variety of structures (Figure S3) [67]. In wood, cellulose chains are produced and aligned enzymatically by cellulose synthase rosette complexes, whereas in this study, the alignment of cellulose was driven by the direction of ice crystal growth. Previous studies on the ice templating of cellulose microfibrils indicated an alignment change from a crosslinked network to a lamellar channel structure with increasing thickness of the lamellae walls as the concentration of microfibrils was increased [68].

This lamellar morphology has also been observed with cryo-cast CNC-polyvinyl alcohol mixtures [69], where microstructure and pore morphology were fine-tuned by modifying the freezing rate and concentration of the components [70].

### 3.4. Translational Cryostage

To better understand the differences in sample morphologies, we analyzed the ice crystal growth using a custom-built motorized translational cryo-stage that enables real time observation of directional freezing/ice crystal growth using optical microscopy [54,71]. Inks were deposited onto a glass slide and covered with a cover slip. The bottom of the slide was in contact with copper plates at its left and right sides, with a central unobscured viewing window. The temperatures of the copper plates were fixed at specific values such that a constant  $\Delta T$  ( $T_{\text{hot}} = 1\text{ }^{\circ}\text{C}$ ,  $T_{\text{cold}} = -3\text{ }^{\circ}\text{C}$ ) was maintained at  $4\text{ }^{\circ}\text{C}$  between the plates (Figure 6a).

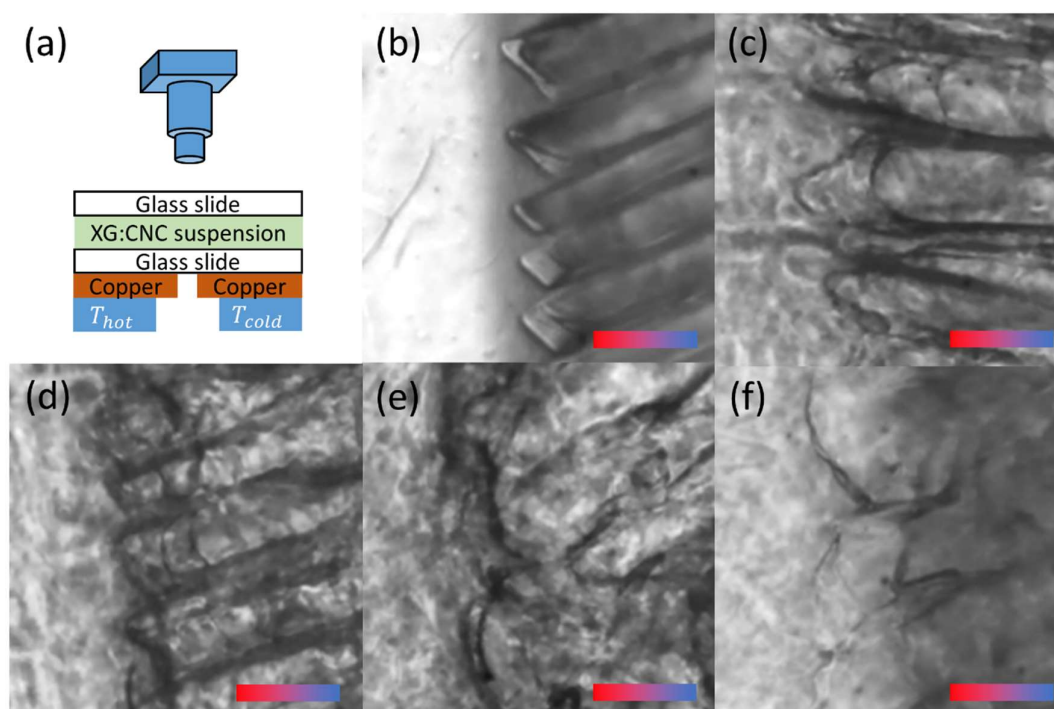


**Figure 6.** Directional freezing experiment: (a) schematic description of the translational cryostage with a fixed  $\Delta T$  ( $T_{\text{hot}} = 1\text{ }^{\circ}\text{C}$ ,  $T_{\text{cold}} = -3\text{ }^{\circ}\text{C}$ ), and (b–f) microscope observation of samples at different XG:CNC ratios of 0:1, 1:100, 1:50, 1:10, and 1:4, respectively. Temperature gradient is shown in scale bars (100  $\mu\text{m}$ , red = hot, blue = cold).

All samples underwent ice growth from the cold side of the slide, while no ice crystals were present in the dispersion at the warm side (Figure 6). The ice crystals in the pure CNC dispersion (Figure 6b) appeared rectangular with an average width of 60  $\mu\text{m}$ , which corresponds well to the features observed by SEM imaging. Moreover, the growth front of the ice crystals appeared straight. As more XG was added, the rectangular ice crystals became rounder, wider, and more tubular in shape (Figure 6c,d), until at high XG contents (1:10 and 1:4 XG:CNC ratios), the ice lacked a clear crystal structure (Figure 6e,f), similar to the morphologies observed of the aerogels using cross-sectional SEM (Figures 4 and 5).

Freeze casting requires that two main conditions are met: (1) particles are rejected from the growing ice front, and (2) the ice front has a non-planar morphology [72], both of which are met in the current study. Several parameters may affect the interaction between the ice front and the particles, including the size and polydispersity of the particles, as well as their shape, surface roughness, and surface energy. In addition, additives may affect the viscosity and surface tension of the liquid, resulting

in different microstructures [73,74]. In the current work, the system was composed of dispersed nanoparticles (CNCs) and a dissolved polymer in water. These samples have different viscosities (Figure 2), which may have affected the crystallization process. Zhou et al. observed ice crystals widening in porous hydroxyapatite, occurring with a concurrent increase in viscosity due to small particle size [75]. This is also similar to the current work, as we have found that added XG increased the viscosity of CNC dispersions and also gave wider ice crystals (Figure 6), which generally resulted in larger pore sizes in the final aerogel (Figures 4 and 5).

Hausmann et al. recently published a paper that evaluated particle alignment in a high concentration CNC suspension by studying the rheology and flow in a needle [76]. This study led to a model that proposed guidelines for designing inks for the alignment of particles. In our case, since the direction of alignment matched that of the ice crystal growth, and since the concentration of CNC was comparatively low, it seems that the most significant parameter for the alignment was the ice templating.

### 3.5. Mechanical Properties

The DCW samples were kept frozen until lyophilization. The mechanical properties of the resultant 3D aerogel objects were evaluated using unconfined compression tests of cylindrical samples (Figure 7). The stress–strain behavior of all samples was typical of elastomeric foams: initially, a linear elastic region was observed due to reversible compression of the foam walls, followed by a short plateau (not apparent in all samples), and finally a sharp linear rise in stress due to irreversible densification until the limits of the load cell were reached. Although the short plateau region was not seen in all samples, the overall trend of increasing modulus with increasing XG content was observed in all samples. The plateau may be related to the contribution of gas pressure within closed cells [1]. As more XG was present, the modulus of the aerogels increased, except for the 1:100 XG:CNC ratio, probably due to its irregular pore structure. Overall, the results indicate that an increase in modulus of over 70% could be achieved by including XG into CNC aerogels. Moreover, the 0:1 and 1:4 XG:CNC ratios seemed to tend toward elastoplastic behavior, as inferred from the apparent yield stress seen in the stress–strain curve.

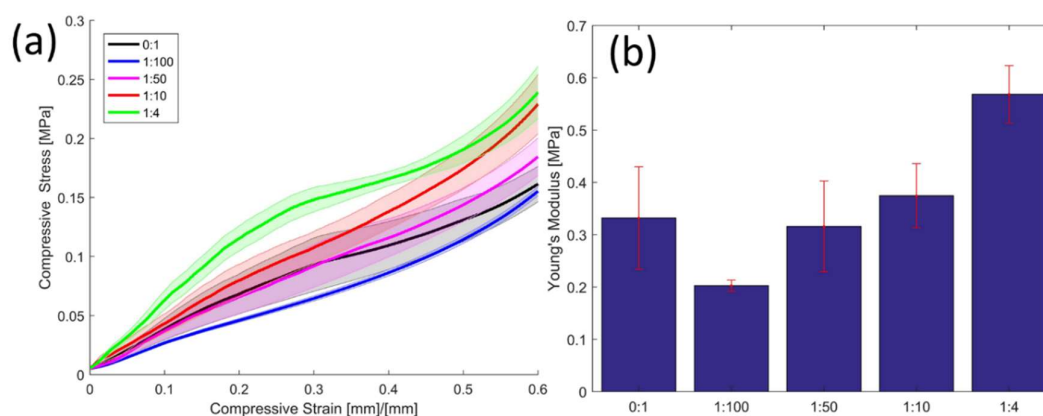


**Figure 7.** Unconfined compression testing of aerogels: (a) stress–strain curves and (b) compressive Young's modulus calculated from the linear elastic range of the stress–strain plot. Legend indicates the ratio of XG:CNC.

Finally, one of the great advantages of DCW is the ability to print objects at angles above 90° relative to the build platform (printing “overhang structure”) without the typical requirement to use an additional support material, thus eliminating the need for post-printing processing to remove the support material. Indeed, a printed vase structure, with angles of  $\approx 120^\circ$  was printed without support, demonstrating this advantage (Figure 8). We note that the fabrication of 3D aerogels was reported for materials such as graphene [77,78], where the objects were obtained via printing

aqueous dispersions, with water removal by lyophilization. However, this process, which results in separate layers, is different than the freeze casting and printing under the feedback-controlled freezing process used herein, which leads to formation of objects with continued long-range alignment of the dispersed particles.



**Figure 8.** 3D DCW of 1:50 XG:CNC frozen vase with  $\approx 120^\circ$  angles, printed directly without using a support material.

#### 4. Conclusions

We presented a new approach for plant cell inspired 3D printing by extrusion-based direct cryo writing. The XG:CNC ink compositions contain plant cell wall components that result in structures that mimic the organization within the plant cell wall due to directional freezing. Extrusion-based 3D printing onto a cold plate with thermal monitoring and on-line temperature control enabled the printing of water-based inks of different XG:CNC ratios and relatively low solid contents. The freezing process was accomplished by proper coordination between the printing flowrate and the freezing rate, such that the two upper layers of the material remained unfrozen, while the material bulk was frozen. This feature is key for enabling the layers to cohesively meld, giving an overall uniform material with no filamentous features. Alignment of the resultant aerogel objects was generated from the freeze casting, while XG:CNC ratios controlled the architecture. The main roles of the CNCs were to impart the shear-thinning rheological behavior needed for the printing process, whereas the XG acted as a binder to improve mechanical properties and to induce internal structure modifications to the 3D printed construction.

We expect that this study will pave the way to the fabrication of 3D objects with controlled internal morphologies, and consequently controlled mechanical properties.

**Supplementary Materials:** The following are available online. Figure S1: Photograph of 3D printed pure CNC cylinders pre-freezing, Figure S2: SEM cross-section, Figure S3: Scanning electron micrographs of wood.

**Author Contributions:** Investigation, D.K., M.C. and C.N.; Supervision, T.A., I.B., S.M. and O.S.

**Funding:** This study was financially supported by the Minerva Center for biohybrid complex systems.

**Acknowledgments:** The authors thank E. Zelinger for technical help with the SEM imaging. The Harvey M. Krueger Family Centre for Nanoscience and Nanotechnology of the Hebrew University is acknowledged.

**Conflicts of Interest:** The authors declare no conflict of interest.

#### References

1. Gibson, L.J.; Ashby, M.F. *Cellular Solids: Structure and Properties*, 2nd ed.; Cambridge University Press: Cambridge, UK, 1999; ISBN 0521499119.
2. Klemm, D.; Heublein, B.; Fink, H.P.; Bohn, A. Cellulose: Fascinating biopolymer and sustainable raw material. *Angew. Chem. Int. Ed.* **2005**, *44*, 3358–3393. [[CrossRef](#)] [[PubMed](#)]
3. Saha, B.C. Hemicellulose bioconversion. *J. Ind. Microbiol. Biotechnol.* **2003**, *30*, 279–291. [[CrossRef](#)] [[PubMed](#)]

4. Miedes, E.; Vanholme, R.; Boerjan, W.; Molina, A. The role of the secondary cell wall in plant resistance to pathogens. *Front. Plant Sci.* **2014**, *5*, 1–13. [[CrossRef](#)] [[PubMed](#)]
5. Deville, S.; Saiz, E.; Nalla, R.K.; Tomsia, A.P. Freezing as a Path to Build Complex Composites. *Science* **2006**, *311*, 515–518. [[CrossRef](#)] [[PubMed](#)]
6. Liu, R.; Xu, T.; Wang, C. A review of fabrication strategies and applications of porous ceramics prepared by freeze-casting method. *Ceram. Int.* **2016**, *42*, 2907–2925. [[CrossRef](#)]
7. Gutiérrez, M.C.; Ferrer, M.L.; Del Monte, F. Ice-templated materials: Sophisticated structures exhibiting enhanced functionalities obtained after unidirectional freezing and ice-segregation-induced self-assembly. *Chem. Mater.* **2008**, *20*, 634–648. [[CrossRef](#)]
8. Wicklein, B.; Kocjan, A.; Salazar-Alvarez, G.; Carosio, F.; Camino, G.; Antonietti, M.; Bergström, L. Thermally insulating and fire-retardant lightweight anisotropic foams based on nanocellulose and graphene oxide. *Nat. Nanotechnol.* **2015**, *10*, 277–283. [[CrossRef](#)] [[PubMed](#)]
9. Wang, Y.; Kong, D.; Shi, W.; Liu, B.; Sim, G.J.; Ge, Q.; Yang, H.Y. Ice Templated Free-Standing Hierarchically WS<sub>2</sub>/CNT-rGO Aerogel for High-Performance Rechargeable Lithium and Sodium Ion Batteries. *Adv. Energy Mater.* **2016**, *6*, 1–9. [[CrossRef](#)]
10. Munch, E.; Launey, M.E.; Alsem, D.H.; Saiz, E.; Tomsia, A.P.; Ritchie, R.O. Tough, Bio-Inspired Hybrid Materials. *Science* **2008**, *322*, 1516–1520. [[CrossRef](#)]
11. Liu, T.; Huang, M.; Li, X.; Wang, C.; Gui, C.X.; Yu, Z.Z. Highly compressible anisotropic graphene aerogels fabricated by directional freezing for efficient absorption of organic liquids. *Carbon N. Y.* **2016**, *100*, 456–464. [[CrossRef](#)]
12. Deville, S.; Saiz, E.; Tomsia, A.P. Freeze casting of hydroxyapatite scaffolds for bone tissue engineering. *Biomaterials* **2006**, *27*, 5480–5489. [[CrossRef](#)] [[PubMed](#)]
13. Fratzl, P.; Weinkamer, R. Nature's hierarchical materials. *Prog. Mater. Sci.* **2007**, *52*, 1263–1334. [[CrossRef](#)]
14. Rees, A.; Powell, L.C.; Chinga-Carrasco, G.; Gethin, D.T.; Syverud, K.; Hill, K.E.; Thomas, D.W. 3D Bioprinting of Carboxymethylated-Periodate Oxidized Nanocellulose Constructs for Wound Dressing Applications. *Biomed Res. Int.* **2015**, *2015*, 1–7. [[CrossRef](#)]
15. Xu, C.; Zhang Molino, B.; Wang, X.; Cheng, F.; Xu, W.; Molino, P.; Bacher, M.; Su, D.; Rosenau, T.; Willför, S.; et al. 3D printing of nanocellulose hydrogel scaffolds with tunable mechanical strength towards wound healing application. *J. Mater. Chem. B* **2018**, *6*, 7066–7075. [[CrossRef](#)]
16. Markstedt, K.; Mantas, A.; Tournier, I.; Martínez Ávila, H.; Hägg, D.; Gatenholm, P. 3D Bioprinting Human Chondrocytes with Nanocellulose–Alginate Bioink for Cartilage Tissue Engineering Applications. *Biomacromolecules* **2015**, *16*, 1489–1496. [[CrossRef](#)] [[PubMed](#)]
17. Sultan, S.; Mathew, A. 3D printed scaffolds with gradient porosity based on cellulose nanocrystal hydrogel. *Nanoscale* **2018**, *10*, 4421–4431. [[CrossRef](#)]
18. Xia, H.; Zhao, D.; Zhu, H.; Hua, Y.; Xiao, K.; Xu, Y.; Liu, Y.; Chen, W.; Liu, Y.; Zhang, W.; et al. Lyophilized Scaffolds Fabricated from 3D-Printed Photocurable Natural Hydrogel for Cartilage Regeneration. *ACS Appl. Mater. Interfaces* **2018**, *10*, 31704–31715. [[CrossRef](#)] [[PubMed](#)]
19. Voisin, H.P.; Gordeyeva, K.; Siqueira, G.; Hausmann, M.K.; Studart, A.R.; Bergström, L. 3D Printing of Strong Lightweight Cellular Structures Using Polysaccharide-Based Composite Foams. *ACS Sustain. Chem. Eng.* **2018**, *6*, 17160–17167. [[CrossRef](#)]
20. Yang, X.; Shi, K.; Zhitomirsky, I.; Cranston, E.D. Cellulose Nanocrystal Aerogels as Universal 3D Lightweight Substrates for Supercapacitor Materials. *Adv. Mater.* **2015**, *27*, 6104–6109. [[CrossRef](#)]
21. De France, K.J.; Hoare, T.; Cranston, E.D. Review of Hydrogels and Aerogels Containing Nanocellulose. *Chem. Mater.* **2017**, *29*, 4609–4631. [[CrossRef](#)]
22. Abitbol, T.; Rivkin, A.; Cao, Y.; Nevo, Y.; Abraham, E.; Ben-Shalom, T.; Lapidot, S.; Shoseyov, O. Nanocellulose, a tiny fiber with huge applications. *Curr. Opin. Biotechnol.* **2016**, *39*, 76–88. [[CrossRef](#)]
23. Scheller, H.V.; Ulvskov, P. Hemicelluloses. *Annu. Rev. Plant Biol.* **2010**, *61*, 263–289. [[CrossRef](#)]
24. Beck-Candanedo, S.; Roman, M.; Gray, D.G. Effect of reaction conditions on the properties and behavior of wood cellulose nanocrystal suspensions. *Biomacromolecules* **2005**, *6*, 1048–1054. [[CrossRef](#)]
25. Kargarzadeh, H.; Ahmad, I.; Abdullah, I.; Dufresne, A.; Zainudin, S.Y.; Sheltami, R.M. Effects of hydrolysis conditions on the morphology, crystallinity, and thermal stability of cellulose nanocrystals extracted from kenaf bast fibers. *Cellulose* **2012**, *19*, 855–866. [[CrossRef](#)]

26. Sacui, I.A.; Nieuwendaal, R.C.; Burnett, D.J.; Stranick, S.J.; Jorfi, M.; Weder, C.; Foster, E.J.; Olsson, R.T.; Gilman, J.W. Comparison of the properties of cellulose nanocrystals and cellulose nanofibrils isolated from bacteria, tunicate, and wood processed using acid, enzymatic, mechanical, and oxidative methods. *ACS Appl. Mater. Interfaces* **2014**, *6*, 6127–6138. [[CrossRef](#)] [[PubMed](#)]
27. Whitney, S.E.C.; Gothard, M.G.E.; Mitchell, J.T.; Gidley, M.J. Roles of Cellulose and Xyloglucan in Determining the Mechanical Properties of Primary Plant Cell Walls. *Plant Physiol.* **1999**, *121*, 657–664. [[CrossRef](#)] [[PubMed](#)]
28. Vincken, J.P.; de Keizer, A.; Beldman, G.; Voragen, A. Fractionation of Xyloglucan Fragments and Their Interaction with Cellulose. *Plant Physiol.* **1995**, *108*, 1579–1585. [[CrossRef](#)] [[PubMed](#)]
29. Hanus, J.; Mazeau, K. The xyloglucan–cellulose assembly at the atomic scale. *Biopolymers* **2006**, *82*, 59–73. [[CrossRef](#)] [[PubMed](#)]
30. Villares, A.; Moreau, C.; Dammak, A.; Capron, I.; Cathala, B. Kinetic aspects of the adsorption of xyloglucan onto cellulose nanocrystals. *Soft Matter* **2015**, *11*, 6472–6481. [[CrossRef](#)] [[PubMed](#)]
31. Benselfelt, T.; Cranston, E.D.; Ondaral, S.; Johansson, E.; Brumer, H.; Rutland, M.W.; Wågberg, L. Adsorption of Xyloglucan onto Cellulose Surfaces of Different Morphologies: An Entropy-Driven Process. *Biomacromolecules* **2016**, *17*, 2801–2811. [[CrossRef](#)] [[PubMed](#)]
32. Cerclier, C.V.; Guyomard-Lack, A.; Cousin, F.; Jean, B.; Bonnin, E.; Cathala, B.; Moreau, C. Xyloglucan–cellulose nanocrystal multilayered films: Effect of film architecture on enzymatic hydrolysis. *Biomacromolecules* **2013**, *14*, 3599–3609. [[CrossRef](#)] [[PubMed](#)]
33. Dammak, A.; Moreau, C.; Azzam, F.; Jean, B.; Cousin, F.; Cathala, B. Influence of cellulose nanocrystals concentration and ionic strength on the elaboration of cellulose nanocrystals–xyloglucan multilayered thin films. *J. Colloid Interface Sci.* **2015**, *460*, 214–220. [[CrossRef](#)] [[PubMed](#)]
34. Munier, P.; Gordeyeva, K.; Bergström, L.; Fall, A.B. Directional Freezing of Nanocellulose Dispersions Aligns the Rod-Like Particles and Produces Low-Density and Robust Particle Networks. *Biomacromolecules* **2016**, *17*, 1875–1881. [[CrossRef](#)]
35. Jiménez-Saelices, C.; Seantier, B.; Cathala, B.; Grohens, Y. Spray freeze-dried nanofibrillated cellulose aerogels with thermal superinsulating properties. *Carbohydr. Polym.* **2017**, *157*, 105–113. [[CrossRef](#)]
36. Josset, S.; Hansen, L.; Orsolini, P.; Griffa, M.; Kuzior, O.; Weisse, B.; Zimmermann, T.; Geiger, T. Microfibrillated cellulose foams obtained by a straightforward freeze–thawing–drying procedure. *Cellulose* **2017**, *24*, 3825–3842. [[CrossRef](#)]
37. Köhnke, T.; Elder, T.; Theliander, H.; Ragauskas, A.J. Ice templated and cross-linked xylan/nanocrystalline cellulose hydrogels. *Carbohydr. Polym.* **2014**, *100*, 24–30. [[CrossRef](#)] [[PubMed](#)]
38. Sehaqui, H.; Salajková, M.; Zhou, Q.; Berglund, L.A. Mechanical performance tailoring of tough ultra-high porosity foams prepared from cellulose I nanofiber suspensions. *Soft Matter* **2010**, *6*, 1824. [[CrossRef](#)]
39. Lavoine, N.; Bergström, L. Nanocellulose-based foams and aerogels: Processing, properties, and applications. *J. Mater. Chem. A* **2017**, *5*, 16105–16117. [[CrossRef](#)]
40. Highley, C.B.; Rodell, C.B.; Burdick, J.A. Direct 3D Printing of Shear-Thinning Hydrogels into Self-Healing Hydrogels. *Adv. Mater.* **2015**, *27*, 5075–5079. [[CrossRef](#)] [[PubMed](#)]
41. Zhu, C.; Han, T.Y.J.; Duoss, E.B.; Golobic, A.M.; Kuntz, J.D.; Spadaccini, C.M.; Worsley, M.A. Highly compressible 3D periodic graphene aerogel microlattices. *Nat. Commun.* **2015**, *6*, 1–8. [[CrossRef](#)] [[PubMed](#)]
42. Pati, F.; Jang, J.; Ha, D.H.; Won Kim, S.; Rhie, J.W.; Shim, J.H.; Kim, D.H.; Cho, D.W. Printing three-dimensional tissue analogues with decellularized extracellular matrix bioink. *Nat. Commun.* **2014**, *5*, 1–11. [[CrossRef](#)] [[PubMed](#)]
43. Lee, S.J.; Kengla, C.; Yoo, J.J.; Atala, A.; Ko, I.K.; Kang, H.-W. A 3D bioprinting system to produce human-scale tissue constructs with structural integrity. *Nat. Biotechnol.* **2016**, *34*, 312–319.
44. Busbee, T.A.; Lewis, J.A.; Kolesky, D.B.; Truby, R.L.; Gladman, A.S.; Homan, K.A. 3D Bioprinting of Vascularized, Heterogeneous Cell-Laden Tissue Constructs. *Adv. Mater.* **2014**, *26*, 3124–3130.
45. Ouyang, L.; Highley, C.B.; Sun, W.; Burdick, J.A. A Generalizable Strategy for the 3D Bioprinting of Hydrogels from Nonviscous Photo-crosslinkable Inks. *Adv. Mater.* **2017**, *29*. [[CrossRef](#)] [[PubMed](#)]
46. Kesti, M.; Müller, M.; Becher, J.; Schnabelrauch, M.; D’Este, M.; Eglin, D.; Zenobi-Wong, M. A versatile bioink for three-dimensional printing of cellular scaffolds based on thermally and photo-triggered tandem gelation. *Acta Biomater.* **2015**, *11*, 162–172. [[CrossRef](#)] [[PubMed](#)]
47. Barry, R.A.; Shepherd, R.F.; Hanson, J.N.; Nuzzo, R.G.; Wiltzius, P.; Lewis, J.A. Direct-write assembly of 3D hydrogel scaffolds for guided cell growth. *Adv. Mater.* **2009**, *21*, 2407–2410. [[CrossRef](#)]

48. Xiong, Z.; Yan, Y.; Wang, S.; Zhang, R.; Zhang, C. Fabrication of porous scaffolds for bone tissue engineering via low-temperature deposition. *Scr. Mater.* **2002**, *46*, 771–776. [[CrossRef](#)]
49. Kim, G.; Ahn, S.; Yoon, H.; Kim, Y.; Chun, W. A cryogenic direct-plotting system for fabrication of 3D collagen scaffolds for tissue engineering. *J. Mater. Chem.* **2009**, *19*, 8817. [[CrossRef](#)]
50. Liao, C.-Y.; Wu, W.-J.; Hsieh, C.-T.; Tseng, C.-S.; Dai, N.-T.; Hsu, S. Design and Development of a Novel Frozen-Form Additive Manufacturing System for Tissue Engineering Applications. *3D Print. Addit. Manuf.* **2016**, *3*, 216–225. [[CrossRef](#)]
51. Adamkiewicz, M.; Rubinsky, B. Cryogenic 3D printing for tissue engineering. *Cryobiology* **2015**, *71*, 518–521. [[CrossRef](#)] [[PubMed](#)]
52. Zhang, Q.; Zhang, F.; Medarametla, S.P.; Li, H.; Zhou, C.; Lin, D. 3D Printing of Graphene Aerogels. *Small* **2016**, *12*, 1702–1708. [[CrossRef](#)] [[PubMed](#)]
53. Song, X.; Tetik, H.; Jirakittsonthon, T.; Parandoush, P.; Yang, G.; Lee, D.; Ryu, S.; Lei, S.; Weiss, M.L.; Lin, D. Biomimetic 3D Printing of Hierarchical and Interconnected Porous Hydroxyapatite Structures with High Mechanical Strength for Bone Cell Culture. *Adv. Eng. Mater.* **2018**, *1800678*, 1–6. [[CrossRef](#)]
54. Bahari, L.; Bein, A.; Yashunsky, V.; Braslavsky, I. Directional freezing for the cryopreservation of adherent mammalian cells on a substrate. *PLoS ONE* **2018**, *13*, 1–17. [[CrossRef](#)]
55. Koppolu, R.; Abitbol, T.; Kumar, V.; Jaiswal, A.K.; Swerin, A.; Toivakka, M. Continuous roll-to-roll coating of cellulose nanocrystals onto paperboard. *Cellulose* **2018**, *25*, 6055–6069. [[CrossRef](#)]
56. Li, M.-C.; Wu, Q.; Song, K.; Lee, S.; Qing, Y.; Wu, Y. Cellulose Nanoparticles: Structure–Morphology–Rheology Relationships. *ACS Sustain. Chem. Eng.* **2015**, *3*, 821–832. [[CrossRef](#)]
57. Shafiei-Sabet, S.; Hamad, W.Y.; Hatzikiriakos, S.G. Rheology of nanocrystalline cellulose aqueous suspensions. *Langmuir* **2012**, *28*, 17124–17133. [[CrossRef](#)] [[PubMed](#)]
58. Siqueira, G.; Kokkinis, D.; Libanori, R.; Hausmann, M.K.; Gladman, A.S.; Neels, A.; Tingaut, P.; Zimmermann, T.; Lewis, J.A.; Studart, A.R. Cellulose Nanocrystal Inks for 3D Printing of Textured Cellular Architectures. *Adv. Funct. Mater.* **2017**, *27*, 1604619. [[CrossRef](#)]
59. Reid, M.S.; Villalobos, M.; Cranston, E.D. Benchmarking Cellulose Nanocrystals: From the Laboratory to Industrial Production. *Langmuir* **2017**, *33*, 1583–1598. [[CrossRef](#)] [[PubMed](#)]
60. Abitbol, T.; Kam, D.; Levi-Kalisman, Y.; Gray, D.G.; Shoseyov, O. Surface Charge Influence on the Phase Separation and Viscosity of Cellulose Nanocrystals. *Langmuir* **2018**, *34*, 3925–3933. [[CrossRef](#)] [[PubMed](#)]
61. Li, V.C.F.; Dunn, C.K.; Zhang, Z.; Deng, Y.; Qi, H.J. Direct Ink Write (DIW) 3D Printed Cellulose Nanocrystal Aerogel Structures. *Sci. Rep.* **2017**, *7*, 1–8. [[CrossRef](#)]
62. Hayashi, T.; Ogawa, K.; Mitsuishi, Y. Characterization of the adsorption of xyloglucan to cellulose. *Plant Cell Physiol.* **1994**, *35*, 1199–1205. [[CrossRef](#)]
63. Levy, S.; Maclachlan, G.; Staehelin, L.A. Xyloglucan sidechains modulate binding to cellulose during in vitro binding assays as predicted by conformational dynamics simulations. *Plant J.* **1997**, *11*, 373–386. [[CrossRef](#)]
64. Eronen, P.; Österberg, M.; Heikkinen, S.; Tenkanen, M.; Laine, J. Interactions of structurally different hemicelluloses with nanofibrillar cellulose. *Carbohydr. Polym.* **2011**, *86*, 1281–1290. [[CrossRef](#)]
65. Cerclier, C.; Cousin, F.; Bizot, H.; Moreau, C.; Cathala, B. Elaboration of spin-coated cellulose-xyloglucan multilayered thin films. *Langmuir* **2010**, *26*, 17248–17255. [[CrossRef](#)] [[PubMed](#)]
66. Chu, G.; Qu, D.; Zussman, E.; Xu, Y. Ice-Assisted Assembly of Liquid Crystalline Cellulose Nanocrystals for Preparing Anisotropic Aerogels with Ordered Structures. *Chem. Mater.* **2017**, *29*, 3980–3988. [[CrossRef](#)]
67. Gibson, L.J. The hierarchical structure and mechanics of plant materials. *J. R. Soc. Interface* **2012**, *9*, 2749–2766. [[CrossRef](#)]
68. Lee, J.; Deng, Y. The morphology and mechanical properties of layer structured cellulose microfibril foams from ice-templating methods. *Soft Matter* **2011**, *7*, 6034. [[CrossRef](#)]
69. Abitbol, T.; Johnstone, T.; Quinn, T.M.; Gray, D.G. Reinforcement with cellulose nanocrystals of poly(vinyl alcohol) hydrogels prepared by cyclic freezing and thawing. *Soft Matter* **2011**, *7*, 2373. [[CrossRef](#)]
70. Dash, R.; Li, Y.; Ragauskas, A.J. Cellulose nanowhisker foams by freeze casting. *Carbohydr. Polym.* **2012**, *88*, 789–792. [[CrossRef](#)]
71. Rubinsky, B.; Ikeda, M. A cryomicroscope using directional solidification for the controlled freezing of biological material. *Cryobiology* **1985**, *22*, 55–68. [[CrossRef](#)]
72. Deville, S. Freeze-Casting of Porous Ceramics: A Review of Current Achievements and Issues. *Adv. Eng. Mater.* **2008**, *10*, 155–169. [[CrossRef](#)]

73. Zhang, Y.; Hu, L.; Han, J.; Jiang, Z. Freeze casting of aqueous alumina slurries with glycerol for porous ceramics. *Ceram. Int.* **2010**, *36*, 617–621. [[CrossRef](#)]
74. Lebreton, K.; Rodríguez-Parra, J.M.; Moreno, R.; Nieto, M.I. Effect of additives on porosity of alumina materials obtained by freeze casting. *Adv. Appl. Ceram.* **2015**, *114*, 296–302. [[CrossRef](#)]
75. Zhou, K.; Zhang, Y.; Zhang, D.; Zhang, X.; Li, Z.; Liu, G.; Button, T.W. Porous hydroxyapatite ceramics fabricated by an ice-templating method. *Scr. Mater.* **2011**, *64*, 426–429. [[CrossRef](#)]
76. Hausmann, M.K.; Rühls, P.A.; Siqueira, G.; Läuger, J.; Libanori, R.; Zimmermann, T.; Studart, A.R. Dynamics of Cellulose Nanocrystal Alignment during 3D Printing. *ACS Nano* **2018**, *12*, 6926–6937. [[CrossRef](#)]
77. Jiang, Y.; Xu, Z.; Huang, T.; Liu, Y.; Guo, F.; Xi, J.; Gao, W.; Gao, C. Direct 3D Printing of Ultralight Graphene Oxide Aerogel Microlattices. *Adv. Funct. Mater.* **2018**, *28*, 1–8. [[CrossRef](#)]
78. Rocha, V.G.; García-Tuñón, E.; Botas, C.; Markoulidis, F.; Feilden, E.; D'Elia, E.; Ni, N.; Shaffer, M.; Saiz, E. Multimaterial 3D Printing of Graphene-Based Electrodes for Electrochemical Energy Storage Using Thermoresponsive Inks. *ACS Appl. Mater. Interfaces* **2017**, *9*, 37136–37145. [[CrossRef](#)] [[PubMed](#)]



© 2019 by the authors. Licensee MDPI, Basel, Switzerland. This article is an open access article distributed under the terms and conditions of the Creative Commons Attribution (CC BY) license (<http://creativecommons.org/licenses/by/4.0/>).